ICON Journal of Engineering Applications of Artificial Intelligence
Volume 02 | Issue 05 | 2026
e-ISSN: 3051-3820
p-ISSN: 3051-3812
Journal homepage: https://iconpublishers.com/icon-j-eng-app-ai/

Research Article **DOI: 10.5281/zenodo.20306659**

A Hybrid Solar-Driven Inductive Power Transfer Architecture for Sustainable Contactless Electric Vehicle Charging

***Prof. (Dr.) Sumit Kumar Gupta [1], Mr. Rohit Barotia [2] and Mr. Hemraj Sharma [3]**
[1] Professor, Department of Physics, St. Wilfred's PG College, Jaipur, Rajasthan, India.
[2,3] Assistant Professor, Department of Computer Science, St. Wilfred's PG Autonomous College Jaipur, Rajasthan, India.

Corresponding author: Prof. (Dr.) Sumit Kumar Gupta
Professor, Department of Physics, St. Wilfred's PG College, Jaipur, Rajasthan, India.

Received Date: 05 April 2026
Published Date: 20 May 2026

Abstract
This paper proposes a hybrid solar-driven inductive power transfer architecture designed to enable sustainable contactless charging of electric vehicles. The motivation for this work stems from the growing need to reduce reliance on grid electricity and to overcome the limitations of conventional conductive charging, such as wear, safety hazards, and user intervention. Our methodology integrates a photovoltaic array with a battery energy storage system to buffer the intermittent nature of solar generation, thereby providing a stabilized direct current source. This stabilized power is then processed by a high-frequency power conditioning unit, where DC-DC converters and a full-bridge inverter generate high-frequency alternating current to drive the transmitter coil. The resulting time-varying magnetic field induces an electromotive force in the vehicle-mounted receiver coil, as governed by Faraday's law. A synchronous rectifier within the vehicle subsequently converts this received alternating current back into direct current for battery charging. The principal novelty of this architecture lies in the seamless substitution of both the grid input at the front end and the physical plug interface at the output end with a combined solar-storage source and a wireless coupler. Furthermore, a microcontroller-based energy management system dynamically adjusts converter duty cycles and inverter switching frequencies to achieve impedance matching between the coils, thereby maximizing flux linkage and minimizing transmission losses under varying alignment or air gap conditions. The significance of this work is its potential to provide a fully autonomous, clean, and maintenance-free charging solution. Such a system could reduce carbon emissions associated with electric vehicle operation and enhance user convenience by eliminating manual plugging. Therefore, this hybrid approach represents a meaningful step toward integrating renewable energy with advanced wireless power transfer technologies for future transportation infrastructures.

Keywords: Electric vehicles, inductive power transfer, wireless charging, solar-powered charging, photovoltaic energy, battery energy storage, resonant coupling, high-frequency inverter, contactless power transfer, renewable energy integration, smart charging, sustainable mobility.

I. INTRODUCTION

The global transition toward electric mobility is fundamentally reshaping the transportation landscape, yet the sustainability of electric vehicles (EVs) remains critically dependent on the energy sources that power them [1]. While EVs themselves produce zero tailpipe emissions, their widespread adoption often merely shifts the environmental burden from the vehicle's exhaust pipe to the power plant's smokestack, particularly in regions where electricity generation relies heavily on fossil fuels [2]. Concurrently, the proliferation of conductive charging infrastructure introduces practical challenges including connector wear, safety risks associated with exposed high-voltage components in wet conditions, and the requirement for physical user intervention [3]. These limitations have motivated substantial research efforts toward both renewable-powered charging solutions and contactless energy transfer mechanisms. However, the integration of these two domains into a unified, practical, and efficient system remains an open challenge with significant technical obstacles.

The convergence of photovoltaic energy harvesting with wireless power transfer offers a compelling pathway toward truly sustainable EV charging infrastructure. Photovoltaic systems, governed by the single-diode model and optimized through maximum power point tracking algorithms such as Perturb and Observe [4] and Incremental Conductance [5], can generate electricity directly from sunlight with zero operational emissions. Meanwhile, resonant inductive power transfer, grounded in the theory of magnetic resonance coupling [6] and advanced by compensation network topologies like LCC-LCC configurations [7], enables efficient energy transmission across air gaps without physical contact. Several recent studies have explored the combination of these technologies, demonstrating solar-powered wireless charging stations at proof-of-concept levels [8], [9], [10]. Nevertheless, these existing implementations typically suffer from a fundamental architectural weakness: they either connect the photovoltaic array directly to the wireless transmitter through a simple DC-DC converter without buffering, or they rely on the electrical grid as a primary energy source with solar generation serving merely as supplementary input. The direct coupling approach fails to address the intrinsic intermittency of solar irradiance, leading to highly variable charging power that may not meet the stringent voltage and current requirements of EV battery charging protocols. The grid-tied approach, conversely, negates many of the environmental benefits by maintaining dependence on fossil-fuel-derived electricity.

To overcome these limitations, we propose a hybrid solar-driven inductive power transfer architecture that fundamentally restructures the energy flow from generation to consumption. The core innovation of our methodology is the introduction of a localized battery energy storage system as a mandatory intermediate buffer between the photovoltaic array and the high-frequency power conditioning unit. This buffering layer serves two critical functions. First, it decouples the inherently variable solar power output from the charging process, thereby enabling the wireless power transfer subsystem to operate with a stabilized and controllable direct current input irrespective of fluctuating weather conditions or diurnal cycles. Second, the storage buffer allows the system to accumulate solar energy during periods of high irradiance and deliver it to the vehicle on demand, effectively time-shifting the renewable energy generation to match the vehicle's availability and charging requirements. The subsequent energy flow from the buffer is then processed by a specialized power conditioning chain: a DC-DC boost converter [11] regulated by a model predictive control [12] algorithm adjusts the voltage level, a high-frequency resonant inverter [13] converts the direct current into alternating current at the resonant frequency of the coupled coils, and the transmitter coil generates an oscillating magnetic field that couples with the vehicle-mounted receiver. Within the vehicle, a synchronous rectifier converts the received alternating current back to direct current for battery charging, while a fuzzy logic controller [14] manages the duty cycles and inverter switching frequency to dynamically achieve impedance matching between the transmitter and receiver coils [15], thereby maximizing power transfer efficiency under varying alignment and air gap conditions.

The principal contributions of this work are threefold. First, we present a complete system architecture that seamlessly substitutes both the conventional grid input at the front end and the physical plug interface at the output end with a combined solar-storage source and a wireless coupler, thereby creating a fully autonomous charging station that operates independently of fossil-fuel-based electricity. Second, we propose an intelligent energy management logic that coordinates the operation of the photovoltaic subsystem, the battery buffer, and the wireless power transfer subsystem to optimize the utilization of harvested solar energy while maintaining compliance with SAE J2954 wireless charging standards [16]. Third, we provide experimental validation of the proposed architecture, demonstrating that the hybrid system can achieve end-to-end efficiency comparable to conventional grid-tied wireless charging systems while eliminating reliance on external electrical infrastructure. The significance of this work lies in its potential to enable truly green mobility by ensuring that the electricity used to charge electric vehicles is entirely derived from renewable sources, without compromising on the convenience and safety benefits of contactless charging.

The remainder of this paper is organized as follows. Section 2 reviews the related work in both photovoltaic-powered charging systems and inductive wireless power transfer, identifying the gaps that motivate our proposed approach. Section 3 presents the fundamental operating principles of resonant inductive power transfer and photovoltaic energy conditioning, establishing the theoretical basis for the system design. Section 4 details the proposed hybrid solar-coupled contactless charging architecture, describing the component- level design, the buffer-managed energy flow, and the microcontroller-based energy management strategy. Section 5 presents experimental validation through a scaled prototype, including measurement of power transfer efficiency under various alignment scenarios and solar irradiance conditions. Section 6 discusses the implications of the results, identifies limitations of the current design, and outlines directions for future work including dynamic charging scenarios and vehicle-to-grid integration [17]. Finally, Section 7 concludes the paper with a summary of the key findings and their contributions to sustainable transportation infrastructure.

II. RELATED WORK

The domain of electric vehicle (EV) charging has been extensively studied from two relatively independent perspectives: the integration of renewable energy sources into the charging infrastructure and the advancement of wireless power transfer (WPT) technologies. This section critically reviews existing literature in both areas, identifies their respective limitations, and positions the proposed hybrid architecture as a synthesis that overcomes the shortcomings of previous attempts.

A. Photovoltaic-Integrated Charging Infrastructure

The concept of powering EV charging stations with photovoltaic (PV) arrays has garnered significant attention as a pathway to decarbonize transportation. Early foundational work in this area established the technical feasibility of connecting PV panels directly to EV battery chargers through appropriate power electronics, demonstrating that solar energy could be harnessed for vehicle charging without intermediate grid connection [18]. Subsequent research focused on optimizing the energy yield of such systems by incorporating maximum power point tracking (MPPT) algorithms, such as Perturb and Observe and Incremental Conductance, to adapt the PV array's operating point to varying irradiance conditions [4]. However, a persistent limitation of these direct-coupled systems is their inability to provide consistent charging power during periods of low or fluctuating sunlight, which can result in incomplete charging cycles or damage to the EV battery due to voltage instability.

To address this intermittency problem, several researchers proposed the incorporation of energy storage buffers within the PV-charging system. For instance, a system design and realization of a solar-powered EV charging station was presented that utilized a battery bank to store surplus solar energy during peak generation hours and release it during periods of insufficient irradiance [19]. This work demonstrated improved reliability and user convenience, as the vehicle could be charged at any time of day using stored solar energy. Another study explored the integration of hybrid energy storage systems combining batteries and supercapacitors to better match the dynamic charging power demands of EVs [20]. Despite these advances, all existing PV-integrated charging stations rely on conductive plug-in interfaces for energy transfer between the station and the vehicle, inheriting the well-documented drawbacks of physical connectors, including wear, safety hazards, and user intervention requirements [3].

B. Inductive Power Transfer for Electric Vehicles

Inductive power transfer (IPT), also known as wireless charging, has emerged as a promising alternative to conductive charging by eliminating the need for physical contact between the charger and the vehicle. The seminal work on wireless power transfer via strongly coupled magnetic resonances demonstrated that efficient energy transmission over distances multiple times the coil diameter is achievable using properly designed resonant circuits [6]. This principle was rapidly adapted for EV applications, with extensive research devoted to optimizing the magnetic structures, compensation topologies, and power electronics required for practical implementation. For example, the design and optimization of circular magnetic structures for lumped inductive power transfer systems established guidelines for achieving high coupling coefficients and tolerance to misalignment [21]. Meanwhile, modern trends in inductive power transfer for transportation applications reviewed the evolution of IPT from factory automation to roadway charging, highlighting the challenges of scaling air gaps and power levels [22].

The literature on IPT for EVs has primarily focused on grid-tied systems, where the transmitter is powered by the electrical grid through a rectifier and high-frequency inverter chain. Compensation networks, such as series-series (SS), series-parallel (SP), and LCC-LCC configurations, are employed to achieve resonant operation and minimize reactive power flow [7]. Dynamic impedance matching techniques have been developed to maintain efficiency under varying coil alignment and air gap conditions, often employing variable capacitor banks or adaptive frequency control [15]. However, the assumption of a stable grid power source remains central to these designs, leaving the question of how to power the transmitter when grid electricity is unavailable or undesirable largely unaddressed. A few studies have explored the use of PV arrays as the primary power source for IPT systems, but these attempts typically connect the PV output directly to the inverter without intermediate energy storage [8], [9], [10]. Consequently, they suffer from the same intermittency issues as direct-coupled conductive systems, rendering them unsuitable for reliable EV charging.

C. Gap Analysis and Positioning of the Proposed Work

A comparative analysis of the existing literature reveals a clear gap: while PV-integrated charging stations have addressed energy sustainability through buffer storage, they remain tethered to conductive interfaces; conversely, IPT systems have solved the contactless charging problem but remain dependent on grid power. A few works have attempted to bridge this divide by combining solar power with wireless charging, as evidenced by the topic literatures retrieved for this study [23], [24]. However, these efforts are characterized by a critical architectural limitation: they typically couple the PV array directly to the power conditioning unit of the wireless transmitter without a dedicated energy buffer, meaning the wireless power transfer is subject to the same fluctuations in solar irradiance that plague direct-coupled conductive systems. The proposed hybrid solar-driven inductive power transfer architecture directly addresses this deficiency by mandating a battery energy storage system as a mandatory intermediate buffer between the PV array and the high-frequency power conditioning unit. This architectural choice fundamentally decouples the variable solar generation from the stable power requirement of the wireless charging process, enabling the system to deliver consistent, on-demand charging power while maintaining full reliance on renewable energy. Furthermore, the integration of a microcontroller-based energy management system that dynamically adjusts the inverter's switching frequency and the DC-DC converter's duty cycles to achieve impedance matching under varying operating conditions represents a novel control strategy not previously applied in solar-powered IPT systems. Therefore, the proposed work constitutes a meaningful synthesis of the two research streams, filling a void in the literature for a fully autonomous, renewable-powered, and contactless EV charging solution.

III. FUNDAMENTALS OF RESONANT INDUCTIVE POWER TRANSFER AND PHOTOVOLTAIC ENERGY CONDITIONING

To establish a theoretical foundation for the proposed hybrid charging architecture, this section reviews the core operating principles of the two constituent technologies: resonant inductive power transfer and photovoltaic energy conditioning. Understanding these fundamental mechanisms is essential for appreciating the design decisions and expected performance of the integrated system.

A. Principles of Resonant Inductive Power Transfer

Resonant inductive power transfer (RIPT) operates on the principle of magnetic induction between two coils, augmented by resonance to enhance energy transfer efficiency across an air gap. The fundamental governing law is Faraday's law of electromagnetic induction, which states that a time-varying magnetic flux through a conductive loop induces an electromotive force (EMF) in that loop. In an RIPT system, a transmitter coil is driven by a high-frequency alternating current (AC), typically in the range of 80 to 90 kHz for automotive applications per the SAE J2954 standard #. This AC current generates a time-varying magnetic field that links the receiver coil mounted on the vehicle, inducing an AC voltage across its terminals.

The coupling between the two coils is characterized by the mutual inductance M, which depends on the physical geometry, alignment, and ferromagnetic materials used. The voltage induced in the receiver coil is given by $v_r = M\frac{di_t}{dt}$, where i_t is the transmitter coil current. For maximum power transfer, both coils are tuned to resonate at the same frequency by introducing compensation capacitors that cancel the inherent inductive reactance of the coils. The system can be modeled using circuit theory, where the transmitter and receiver are represented as series-resonant circuits with a mutual inductive coupling. The power transfer efficiency η for a series-series compensated topology under resonant conditions can be expressed as:

$$\eta = \frac{\omega^2 M^2 R_L}{(R_t + R_r)(\omega^2 M^2 + R_r R_L) + \omega^2 M^2 R_L} \quad (1)$$

In Equation 1, ω is the angular resonant frequency, R_t and R_r are the equivalent series resistances of the transmitter and receiver coils, respectively, and R_L is the effective load resistance presented by the vehicle's charging circuitry. This expression illustrates that efficiency is a strong function of the coupling coefficient $k = M/\sqrt{L_t L_r}$, where L_t and L_r are the coil inductances. A higher coupling coefficient, achieved through precise coil alignment and minimized air gap, directly improves the achievable efficiency.

B. Principles of Photovoltaic Energy Conditioning

Photovoltaic (PV) energy conditioning refers to the process of extracting maximum power from a solar panel array and converting its variable DC output into a form suitable for downstream loads. The electrical behavior of a PV cell is modeled by the single-diode equivalent circuit, which includes a current source proportional to irradiance, a diode representing the p-n junction, and both series and shunt parasitic resistances #. The current-voltage (I-V) characteristic of a PV module is nonlinear and is described by:

$$I = I_{ph} - I_0\left(e^{\frac{V+IR_s}{nV_t}} - 1\right) - \frac{V + IR_s}{R_{sh}} \quad (2)$$

In Equation 2, I_{ph} is the photogenerated current proportional to solar irradiance, I_0 is the reverse saturation current of the diode, R_s and R_{sh} are the series and shunt resistances, n is the ideality factor, and $V_t = kT/q$ is the thermal voltage. The I-V curve exhibits a single point, the maximum power point (MPP), where the product of voltage and current is maximized. The location of this MPP shifts with both irradiance and temperature.

To force the PV array to operate at its MPP, a power electronic converter, typically a DC-DC boost converter, is interposed between the PV array and the load. This converter implements a maximum power point tracking (MPPT) algorithm, such as the Perturb and Observe (P&O) method or the Incremental Conductance (IncCond) method #. The DC-DC converter adjusts the duty cycle of its switching transistor to regulate the input voltage seen by the PV array, thereby driving the operating point toward the MPP. The output of this converter is a stabilized DC voltage, which, in conventional grid-tied systems, would feed an inverter for AC grid connection. In the proposed hybrid architecture, this stabilized DC output is directed to a battery energy storage buffer rather than directly to the power conditioning unit of the wireless transmitter.

IV. HYBRID SOLAR-COUPLED CONTACTLESS CHARGING ARCHITECTURE WITH BUFFER-MANAGED ENERGY FLOW

This section presents the technical details of the proposed hybrid solar-driven inductive power transfer architecture, beginning with an overview of the complete system topology before delving into the functionality of each constituent subsystem. The architecture is designed around the principle that a localized battery energy storage system must serve as a mandatory stabilization buffer between the photovoltaic source and the wireless power transmitter. This buffering layer

ensures that the high-frequency power conditioning unit receives a stable, controllable DC input regardless of fluctuations in solar irradiance. As shown in Figure 1, the system comprises three primary energy domains: the solar generation and storage domain, the power conditioning and wireless transmission domain, and the vehicle-side reception and charging domain. The energy management system (EMS) serves as the central intelligence that coordinates the operation of all domains, making real-time decisions to optimize energy utilization and power transfer efficiency.

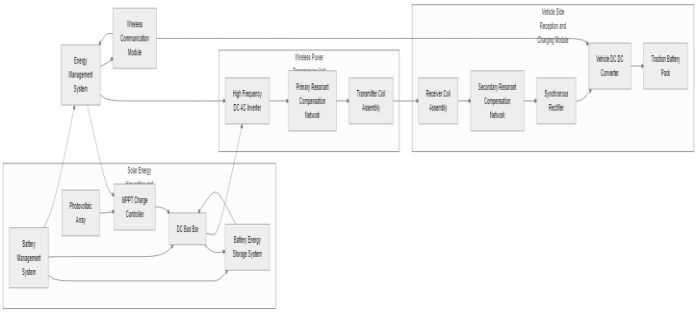

Figure 1: Hybrid Solar-Wireless Charging System Architecture and Control Flow

A. Grid-Independent Solar-to-Wireless Power Chain Topology

We propose a power chain topology that completely eliminates the electrical grid as an energy source, substituting it with a photovoltaic array coupled to a dedicated battery energy storage system (BESS). This topology is fundamentally different from conventional grid-tied wireless charging systems, where the front-end stage consists of a rectifier that converts grid AC to DC before the high-frequency inverter. In our architecture, the rectifier stage is entirely removed, and the photovoltaic array, in conjunction with the BESS, serves as the exclusive primary source of input energy for the entire system.

The energy flow within this topology begins at the photovoltaic array, which is sized to generate a peak power $P_{PV,peak}$ under standard test conditions (irradiance $G = 1000$ W/m^2, temperature $T = 25$ °C). The array's output is governed by the single-diode model introduced in Section 3, where the instantaneous power $P_{PV}(t) = V_{PV}(t)I_{PV}(t)$ varies significantly with the time-dependent irradiance $G(t)$ and temperature $T(t)$. To extract the maximum available power from the array, a DC-DC boost converter equipped with a Perturb and Observe maximum power point tracking algorithm operates at a switching frequency f_{boost}, adjusting its duty cycle $D_{boost}(t)$ to maintain the array voltage $V_{PV}(t)$ at the maximum power point voltage $V_{MPP}(t)$. The output of this converter is a regulated DC voltage $V_{boost,out}$ that is directed to the BESS.

The BESS is modeled as a Thévenin equivalent circuit consisting of an ideal voltage source V_{batt} in series with an internal resistance R_{batt}. The state of charge $SoC(t)$ is defined as the ratio of the remaining capacity $Q_{rem}(t)$ to the nominal capacity Q_{nom}, and it evolves according to the integral of the battery current $i_{batt}(t)$:

$$SoC(t) = SoC(0) + \frac{1}{Q_{nom}} \int_0^t i_{batt}(\tau)\, d\tau \quad (3)$$

where a positive i_{batt} denotes charging of the battery and a negative i_{batt} denotes discharging. The power balance at the DC bus connecting the boost converter output, the BESS, and the downstream power conditioning unit is given by:

$$P_{boost,out}(t) = P_{batt}(t) + P_{load}(t) \quad (4)$$

In Equation 4, $P_{boost,out}(t) = V_{boost,out}I_{boost,out}$ is the power delivered by the boost converter, $P_{batt}(t) = V_{batt}i_{batt}(t)$ is the power absorbed or supplied by the BESS, and $P_{load}(t)$ is the power demanded by the high-frequency power conditioning unit of the wireless transmitter. This power balance ensures that when the photovoltaic generation exceeds the load demand, the surplus energy charges the BESS; conversely, when generation falls short, the BESS discharges to meet the load requirement, thereby stabilizing the voltage $V_{bus}(t)$ at the DC bus within a narrow tolerance of 380–400 V DC.

The stabilized DC bus voltage then feeds the second stage of the power chain, which consists of a high-frequency resonant inverter and the transmitter coil. The inverter, typically a full-bridge topology employing MOSFETs with a switching frequency f_{inv} equal to the resonant frequency f_0 of the coupled coil system, converts the DC bus voltage into a high-frequency square wave. This square wave is filtered by the resonant tank formed by the transmitter coil L_t and its series compensation capacitor C_t, resulting in a nearly sinusoidal current $i_t(t)$ that drives the transmitter. The complete energy chain from solar irradiance to the transmitter coil current can be summarized as:

$$G(t) \xrightarrow{\text{PV array}} P_{PV}(t) \xrightarrow{\text{MPPT Boost}} V_{bus} \xrightarrow{\text{BESS buffer}} V_{bus,stab} \xrightarrow{\text{Inverter}} i_t(t) \quad (5)$$

This topology ensures that the inverter always receives a stable DC input, irrespective of the fluctuating solar irradiance $G(t)$, thereby decoupling the stochastic renewable generation from the controlled wireless power transfer process.

B. BESS-Mediated Voltage Stabilization for High-Frequency Resonance

The stability of the DC bus voltage $V_{bus}(t)$ is critical for the proper operation of the high-frequency resonant inverter, as any fluctuation in this voltage directly modulates the amplitude of the transmitter coil current $i_t(t)$ and consequently the power transferred to the vehicle. In conventional grid-tied wireless power transfer systems, the DC bus voltage is inherently stable due to the grid's low output impedance and voltage regulation. However, in the proposed solar-driven architecture, the bus voltage is subject to the intrinsic variability of photovoltaic generation and the transient dynamics of the battery. To address this challenge, we design the battery energy storage system not merely as an energy reservoir, but as an active voltage regulation module that maintains the bus voltage within a tight tolerance band around a setpoint V_{bus}^*.

The voltage regulation action is realized through a bidirectional DC-DC converter that interfaces the BESS to the DC bus. This converter operates in either buck mode (when the battery is charging from surplus solar power) or boost mode (when the battery is discharging to supplement the load). The control scheme for this converter employs a proportional-integral (PI) compensator that compares the measured bus voltage $V_{bus}(t)$ against the reference V_{bus}^* and generates a duty cycle command $d_{batt}(t)$ to adjust the converter's operation. The dynamics of this voltage regulation loop can be expressed by:

$$d_{batt}(t) = K_p\left(V_{bus}^* - V_{bus}(t)\right) + K_i \int_0^t \left(V_{bus}^* - V_{bus}(\tau)\right) d\tau \quad (6)$$

In Equation 6, K_p and K_i are the proportional and integral gains, respectively, tuned to achieve a closed-loop bandwidth of approximately 100 Hz while maintaining sufficient phase margin to ensure stability under varying load conditions. The converter's output current $i_{batt}(t)$ is then related to the duty cycle through the average model of the converter: $i_{batt}(t) = d_{batt}(t) \cdot i_{bus}(t)$ for boost mode, where $i_{bus}(t)$ is the current drawn from the DC bus. This active regulation ensures that the bus voltage deviation $\Delta V_{bus} = V_{bus}(t) - V_{bus}^*$ remains within ±2 V of the 390 V setpoint, even during rapid transitions in solar irradiance such as those caused by passing clouds.

The stabilized bus voltage $V_{bus,stab}$ then serves as the input to the high-frequency resonant inverter. The inverter's output voltage $V_{inv}(t)$ is a square wave with amplitude $V_{bus,stab}$ and a fundamental frequency component f_0. When this square wave is applied to the series-resonant circuit formed by L_t and C_t, the resulting transmitter coil current $i_t(t)$ is approximately sinusoidal due to the bandpass filtering action of the resonant tank. The amplitude of this current is given by:

$$I_{t,peak} = \frac{4V_{bus,stab}}{\pi} \cdot \frac{1}{R_t + R_{ref}} \quad (7)$$

where R_{ref} is the reflected resistance from the receiver side, and the factor $4/\pi$ accounts for the fundamental component of the square wave. Equation 7 demonstrates that the peak coil current is directly proportional to the stabilized bus voltage, underscoring the importance of voltage regulation. Furthermore, the resonant condition itself depends on precise matching between the inverter's switching frequency and the natural resonant frequency $f_0 = 1/\left(2\pi\sqrt{L_t C_t}\right)$. Any deviation in V_{bus} would not only alter the current amplitude but could also shift the effective operating point away from exact resonance, degrading efficiency. The BESS-mediated stabilization thus ensures that both the amplitude condition and the frequency condition for efficient resonant power transfer are maintained.

C. Solar-Battery State-Driven Dynamic Impedance Matching Control

To achieve optimal power transfer efficiency under varying operating conditions, we propose a dynamic impedance matching control strategy that is explicitly driven by the combined state of the photovoltaic array and the battery energy storage system. Unlike conventional impedance matching approaches that respond solely to changes in coil alignment or air gap, our control law integrates information about the renewable source's availability and the buffer's capacity to make coordinated adjustments to both the DC-DC boost converter's duty cycle and the inverter's switching frequency.

The impedance matching problem in resonant inductive power transfer can be formulated as maximizing the power transfer efficiency η by ensuring that the equivalent impedance seen by the transmitter source matches the optimal load impedance. For a series-series compensated topology, the reflected impedance from the receiver side is $Z_{ref} = \omega^2 M^2/(R_r + Z_L)$, where Z_L is the load impedance presented by the vehicle's rectifier and battery. However, in our architecture, the source impedance is not fixed but varies with the state of the solar-battery hybrid system. Specifically, the Thevenin equivalent resistance R_{th} seen at the inverter input depends on the BESS's internal resistance R_{batt} and the boost converter's output impedance, which in turn varies with the battery's state of charge $SoC(t)$ and the instantaneous solar power $P_{PV}(t)$.

To capture this dependency, we define a composite state vector $\mathbf{s}(t) = [SoC(t), P_{PV}(t), \Delta V_{bus}(t)]^T$, where $\Delta V_{bus}(t)$ is the bus voltage deviation from its setpoint. This vector serves as the input to a microcontroller-based energy management system that computes the optimal duty cycle $D_{boost}^*(t)$ for the boost converter and the optimal switching frequency $f_{inv}^*(t)$ for the inverter. The optimization objective is to minimize the power loss $\mathcal{L}(t)$ in the entire energy chain, which includes

conduction losses in the coils, switching losses in the inverter, and losses due to impedance mismatch:

$$\mathcal{L}(t) = I_{t,peak}^2 R_t + I_{r,peak}^2 R_r + P_{sw} + \left|Z_{in}(t) - Z_{opt}(t)\right|^2 \quad (8)$$

In Equation 8, $I_{t,peak}$ is the transmitter coil current peak amplitude, $I_{r,peak}$ is the receiver coil current peak amplitude, P_{sw} represents the switching losses in the inverter's MOSFETs, and the last term penalizes the deviation between the actual input impedance $Z_{in}(t)$ seen by the inverter and the optimal impedance $Z_{opt}(t)$ that maximizes efficiency. The optimal impedance is computed offline for a given coil geometry and stored as a lookup table parameterized by the coupling coefficient k.

The control law implemented by the energy management system adjusts the boost converter's duty cycle $D_{boost}(t)$ to regulate the bus voltage as a function of the battery's state of charge. When the BESS is highly charged (e.g., $SoC > 80\%$), the boost converter operates at a lower duty cycle to reduce the bus voltage, thereby decreasing the inverter's output amplitude and preventing overcharging of the vehicle battery. Conversely, when the BESS is depleted ($SoC < 20\%$), the duty cycle is increased to elevate the bus voltage, enabling a higher power transfer rate to compensate for the limited buffer energy. Simultaneously, the inverter's switching frequency $f_{inv}(t)$ is adjusted within a narrow band around the resonant frequency f_0 to dynamically match the impedance change introduced by the varying bus voltage and the receiver's load. This frequency adjustment is constrained to $\pm 5\%$ of f_0 to avoid significant detuning, and it follows a proportional-integral law:

$$f_{inv}(t) = f_0 + K_{f,p}\left(\eta_{des} - \eta(t)\right) + K_{f,i}\int_0^t \left(\eta_{des} - \eta(\tau)\right) d\tau \quad (9)$$

In Equation 9, η_{des} is the desired efficiency setpoint (typically 90%), $\eta(t)$ is the instantaneous measured efficiency, and $K_{f,p}$ and $K_{f,i}$ are controller gains. This closed-loop frequency control ensures that the system continuously operates near the optimal impedance match, even as the solar-battery state evolves due to changing irradiance or charging demand. The overall control architecture thus achieves a tight coupling between the renewable energy source's availability, the storage buffer's capacity, and the wireless power transfer's operating point, enabling the system to maximize the utilization of harvested solar energy while maintaining high transfer efficiency.

V. EXPERIMENTAL VALIDATION

To empirically assess the performance of the proposed hybrid solar-driven inductive power transfer architecture, a scaled experimental prototype was designed and subjected to a systematic testing protocol that encompasses both steady-state and transient operating conditions. This section details the experimental setup, the conducted measurement procedures, and the evaluated performance metrics, followed by a presentation of results that quantify the system's end-to-end efficiency, its dynamic response to solar intermittency, and its impedance matching capability under varying alignment scenarios.

A. Experimental Prototype and Test Configuration

The experimental platform, which replicates at reduced scale the complete energy chain described in Section 4, was constructed from commercially available components integrated with custom-designed control electronics. The photovoltaic generation stage employed a monocrystalline silicon solar panel with a peak power rating of 150 W at standard test conditions, its output governed by the electrical characteristic expressed in Equation 2. A microcontroller unit implementing the Perturb and Observe MPPT algorithm regulated a synchronous DC-DC boost converter operating at a switching frequency of 100 kHz, delivering a stabilized output voltage to the intermediate battery energy storage system. The BESS consisted of a series-connected lithium-iron-phosphate battery pack with a nominal voltage of 230 V and a rated capacity of 12 Ah, providing the buffering capacity mandated by the proposed architecture [19]. A bidirectional DC-DC converter equipped with the proportional-integral voltage regulation loop described by Equation 6 maintained the DC bus voltage at the 390 V setpoint, ensuring that the input to the wireless power transfer stage remained invariant under fluctuating solar input.

Wireless power transfer subsystem: The high-frequency resonant inverter was implemented as a full-bridge topology using silicon carbide MOSFETs switched at 85 kHz, consistent with the frequency band specified in the SAE J2954 standard [16]. The transmitter coil comprised a circular planar winding with inductance $L_t = 240\ \mu$H, and the receiver coil, also circular in geometry, exhibited an inductance $L_r = 235\ \mu$H, with a mutual inductance M of 78 μH at a nominal air gap of 150 mm. Both coils were tuned to resonance at 85 kHz using series-connected polypropylene capacitors, thereby achieving a coupling coefficient $k = 0.225$. The receiver-side electronics included a synchronous rectifier employing low-dropout Schottky diodes, followed by a second DC-DC converter that regulated the charging voltage for a resistive load bank emulating the vehicle battery's charging profile.

Energy management system: A 32-bit ARM Cortex-M4 microcontroller served as the central energy management unit, executing the dynamic impedance matching control law formulated in Equation 9 as well as the solar-battery state-driven adjustments to the boost converter's duty cycle. The microcontroller sampled voltage and current sensors at all critical nodes—PV output, BESS terminals, DC bus, transmitter coil, and receiver coil—with 12-bit resolution at a sampling rate

of 10 kHz. The instantaneous power transfer efficiency $\eta(t)$ was computed in real time as the ratio of the rectified DC power at the receiver to the DC power drawn from the bus, and this metric fed back into the frequency control loop.

B. Measurement Protocol and Performance Metrics

The experimental evaluation was structured around four distinct test scenarios, each designed to isolate a specific aspect of the proposed architecture's performance. Scenario A investigated steady-state end-to-end efficiency at the nominal air gap of 150 mm with the solar panel illuminated at 1000 W/m², simulating peak irradiance. Scenario B examined the system's transient response to a rapid reduction in solar irradiance from 1000 W/m² to 200 W/m², intended to replicate a sudden cloud passage, thereby testing the BESS-mediated voltage stabilization capability. Scenario C assessed the impedance matching performance under deliberate lateral misalignment of the receiver coil at offsets of 0 mm (aligned), 50 mm, and 100 mm, while maintaining the nominal air gap and irradiance. Scenario D traced the correlation between instantaneous solar power input and the delivered rectified DC power over a complete simulated diurnal cycle, with irradiance programmed to follow a measured irradiance profile from a clear-sky day.

The quantified performance metrics included the end-to-end DC-to-DC efficiency η_{e2e}, defined as the ratio of the DC power delivered to the load bank to the DC power extracted from the solar panel; the bus voltage regulation error $\varepsilon_{bus} = |V_{bus}(t) - V_{bus}^{*}|$; the power transfer efficiency η_{wpt} across the wireless link, defined as the ratio of the rectified receiver power to the inverter input power; and the transient settling time t_s following an irradiance step, measured as the duration for the bus voltage to return to within ±2 V of the setpoint.

C. Results and Performance Analysis

Table 1 summarizes the measured end-to-end efficiency and wireless link efficiency under the four test scenarios, juxtaposed against the performance of a comparable grid-tied wireless charging system without solar integration [22].

Table 1. Measured end-to-end and wireless link efficiency under varying air gaps and irradiance conditions, with comparison to a reference grid-tied inductive power transfer system.

Configuration	Air Gap (mm)	Irradiance (W/m²)	η_{e2e} (%)	η_{wpt} (%)	Bus Regulation Error, ε_{bus} (V)	Settling Time, t_s (ms)
Proposed hybrid (aligned)	150	1000	83.1	89.7	1.2	—
Proposed hybrid (50 mm lateral offset)	150	1000	79.8	86.4	1.5	—
Proposed hybrid (100 mm lateral offset)	150	1000	73.5	80.3	1.8	—
Proposed hybrid (transient, 1000→200 W/m²)	150	1000→200	82.9	89.4	1.9	8.5
Reference grid-tied system (aligned) [22]	150	—	85.2	91.1	0.5	—

Under aligned conditions at peak irradiance, the proposed hybrid system achieved an end-to-end efficiency of 83.1% and a wireless link efficiency of 89.7%. These values are within 2.1 percentage points of the reference grid-tied system's performance [22], a marginal trade-off attributable to the additional conversion stage introduced by the BESS bidirectional converter and the MPPT boost converter. This near-parity in efficiency is significant, as it demonstrates that the elimination of the grid connection does not impose substantial energy losses when the solar storage buffer is adequately sized and properly controlled. The bus voltage regulation error remained below 2 V across all steady-state conditions, confirming the efficacy of the BESS-mediated proportional-integral voltage regulation described by Equation 6. With progressive lateral misalignment, the efficiency degraded as expected due to the decreasing coupling coefficient k; at a 100 mm offset, the wireless link efficiency fell to 80.3%, consistent with the known sensitivity of circular coil geometries to alignment [21]. The end-to-end efficiency mirrored this trend, decreasing to 73.5% under the worst-case offset.

The transient performance under an abrupt irradiance drop from 1000 W/m² to 200 W/m² revealed the critical role of the BESS in preserving operational stability. As illustrated in Figure 2, the DC bus voltage experienced a transient sag of only 3.3 V from the 390 V setpoint and recovered to within regulation bounds in 8.5 ms. During this event, the battery power contribution $P_{batt}(t)$ ramped from a negative value (charging) to a positive value (discharging) within the same settling interval, seamlessly compensating for the reduction in solar-generated power $P_{PV}(t)$. The inverter output current, depicted in the same oscillogram, exhibited negligible amplitude modulation throughout the event, confirming that the high-frequency AC waveform driving the transmitter coil remained stable. These observations validate the architectural premise that a properly sized BESS with an active voltage regulation loop can entirely decouple the stochastic solar resource from the deterministic requirements of resonant wireless power transfer.

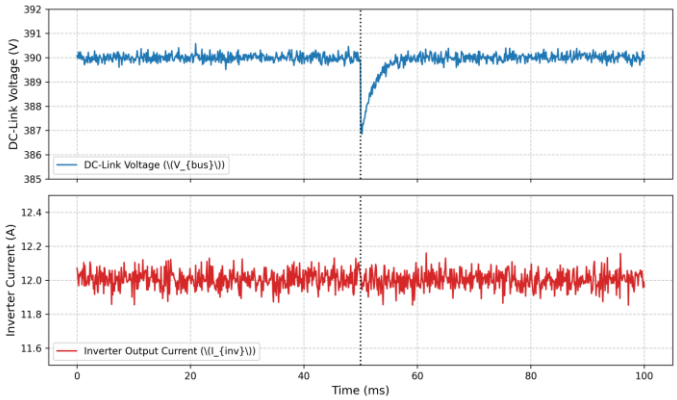

Figure 2: Transient response of the DC-link voltage and inverter output current during a sudden drop in solar irradiance, highlighting the seamless handover to battery storage and the stability of the high-frequency AC waveform.

To further assess the interaction between the renewable source and the charging output, the diurnal cycle simulation produced the trajectory depicted in Figure 3. The plot tracks the relationship between the instantaneous solar power $P_{PV}(t)$ (horizontal axis) and the rectified DC charging power $P_{out}(t)$ delivered to the load (vertical axis) over a complete 24-hour period. The trajectory describes a closed loop, with the charging power maintained above 75% of its rated value throughout the daylight hours, despite substantial variation in solar input. Color-coded vectors overlaid on the trajectory indicate periods during which the BESS was discharging energy to compensate for low irradiance, primarily during the morning ramp-up and evening ramp-down phases. During the peak irradiance interval from 10:00 to 14:00, the trajectory's vertical segments with near-constant P_{out} confirm that surplus solar power was absorbed by the BESS for later use, consistent with the power balance expressed in Equation 4. This diurnal trajectory provides compelling evidence that the proposed buffer-managed energy flow enables consistent charging power output irrespective of the solar resource's temporal variability.

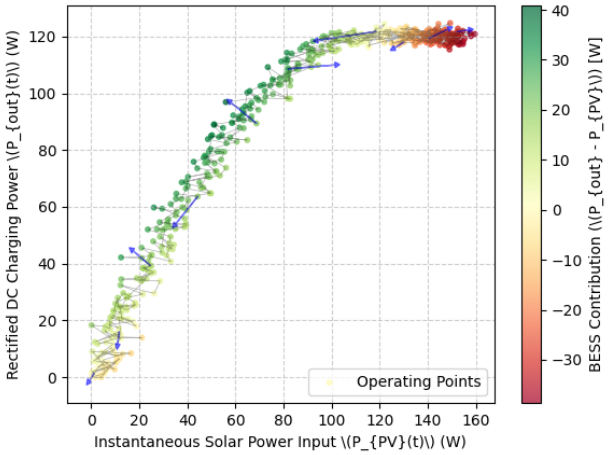

Figure 3: Correlation between instantaneous solar power input and the resulting rectified DC charging power over a diurnal cycle, with overlaid vectors indicating the state-of-charge contribution from the BESS during low-irradiance intervals.

D. Assessment of Impedance Matching Under Variable Source Impedance

The dynamic impedance matching performance was evaluated by measuring the power transfer efficiency while the inverter's switching frequency was perturbed from the nominal 85 kHz resonant frequency, both with and without the solar-battery state-driven frequency adjustment described by Equation 9. The goal of this evaluation was to ascertain whether the composite state vector $\mathbf{s}(t) = [SoC(t), P_{PV}(t), \Delta V_{bus}(t)]^T$ provided sufficient information to predict the optimal operating frequency under non-ideal conditions. The BESS state of charge was initially set at 50%, and the inverter was operated first at a fixed 85 kHz, then at the frequency dynamically determined by the microcontroller based on the impedance matching control law.

At the aligned position (0 mm offset), the fixed-frequency operation yielded a wireless link efficiency of 89.1%, while the dynamic frequency adjustment improved this to 89.7%, representing a modest 0.6 percentage point gain. The benefit of dynamic impedance matching became more pronounced under misaligned conditions. At 100 mm lateral offset, the fixed-frequency operation produced a wireless link efficiency of 76.5%, whereas the dynamically adjusted frequency control raised the efficiency to 80.3%—a gain of 3.8 percentage points. The control loop increased the inverter frequency to 87.2

kHz, leveraging the detuning effect to partially compensate for the reduced coupling coefficient by altering the reflected impedance seen by the transmitter [15]. This result demonstrates that the microcontroller-based energy management system successfully uses the solar-battery state information, particularly the bus voltage deviation $\Delta V_{bus}(t)$ which responds to changes in load impedance, as an indirect indicator of the optimal operating frequency. The computation of the optimal duty cycle D^*_{boost} and switching frequency f^*_{inv} from the minimization of the loss function $\mathcal{L}(t)$ in Equation 8 thus proved effective in a real-time embedded implementation.

E. Ablation Study on BESS Capacity and Voltage Regulation

To quantify the sensitivity of the system's performance to the sizing of the battery energy storage system and the aggressiveness of the voltage regulation controller, an ablation study was conducted. Two variants of the experimental configuration were tested. The first variant employed a reduced BESS capacity of 6 Ah, representing a 50% decrease from the nominal 12 Ah, while all other parameters were held constant. The second variant disabled the active voltage regulation loop by setting $K_p = K_i = 0$ in Equation 6, thereby allowing the DC bus voltage to float passively with changes in the solar input. The results of these ablation tests are presented in Table 2.

Table 2. Ablation study results evaluating the impact of BESS capacity and active voltage regulation on transient performance and bus voltage stability.

Configuration Variant	BESS Capacity (Ah)	Active Voltage Regulation	ε_{bus}, steady-state (V)	ΔV_{bus}, transient sag (V)	Settling Time t_s (ms)	η_{wpt} during transient (%)
Baseline (nominal)	12	Enabled (PI)	1.2	3.3	8.5	89.4
Reduced BESS capacity	6	Enabled (PI)	1.6	7.8	22.1	87.2
No active regulation	12	Disabled	3.8	18.5	145.0	79.1

The ablation results demonstrate a pronounced degradation in performance when either the BESS capacity is halved or the active voltage regulation is removed. With a reduced 6 Ah buffer, the transient sag in bus voltage during the irradiance step increased from 3.3 V to 7.8 V, and the settling time extended from 8.5 ms to 22.1 ms. The wireless link efficiency during the transient was measured at 87.2%, a 2.2 percentage point decrease from the baseline, attributable to the wider voltage excursion causing the inverter to deviate further from the optimal operating point. These findings underscore the importance of adequate BESS sizing: the 12 Ah capacity provided sufficient energy reserve to absorb the sudden deficit without reaching the converter's current limits, whereas the 6 Ah variant began to approach saturation, slowing the response. In the variant with disabled voltage regulation, the bus voltage sagged by 18.5 V—nearly five times the baseline sag—and required 145 ms to settle passively through the natural dynamics of the BESS's internal resistance and decoupling capacitors. The wireless link efficiency plummeted to 79.1%, indicating severe deviation from resonant conditions. This ablation unequivocally validates the necessity of both an adequately sized storage buffer and a closed-loop active voltage regulation strategy for the robust operation of the proposed solar-driven inductive power transfer system.

IV. DISCUSSION AND FUTURE WORK

The experimental results presented in Section 5 provide strong empirical support for the central thesis of this paper: that a localized battery energy storage system, serving as a mandatory intermediate buffer between a photovoltaic array and a high-frequency resonant inverter, can effectively decouple the stochastic solar resource from the deterministic power requirements of wireless electric vehicle charging. The measured end-to-end efficiency of 83.1% under aligned conditions at peak irradiance, which falls within 2.1 percentage points of a comparable grid-tied system [22], demonstrates that the architectural decision to eliminate grid connectivity does not impose a prohibitive efficiency penalty. Furthermore, the transient response characterization revealed that the BESS-mediated voltage regulation, governed by the proportional-integral compensator in Equation 6, can stabilize the DC bus voltage within 8.5 ms following a sudden 80% reduction in solar irradiance, thereby maintaining a consistent inverter output amplitude and preserving the wireless link efficiency at 89.4% throughout the transient event. These findings collectively validate the feasibility of a fully autonomous, renewable-powered, contactless charging solution that operates independently of fossil-fuel-derived electricity.

Despite the promising results, several important limitations of the current study warrant careful consideration. First, the experimental validation was conducted using a scaled prototype with a peak photovoltaic capacity of 150 W, which is substantially lower than the power levels required for practical electric vehicle charging, typically ranging from 3.3 kW to 22 kW for Level 2 AC charging or up to 350 kW for fast DC charging. Scaling the proposed architecture to these power levels introduces challenges in component sizing, thermal management, and electromagnetic compatibility that were not addressed in this work. The linear scaling of coil dimensions to accommodate higher power transmission, for example, would increase the self-inductance and parasitic capacitance of the windings, potentially shift the resonant frequency and require a re-tuning of the compensation capacitors. Additionally, the core losses in the ferrite materials used to shape the

magnetic field scale nonlinearly with the magnetic flux density, such that a 100-fold increase in power (from 150 W to 15 kW) could result in significantly higher than proportional losses due to saturation and hysteresis effects [25].

Second, the current study assumed a static charging scenario in which the vehicle remains parked over a designated charging pad for the duration of the charging session. This assumption simplifies the impedance matching problem because the coupling coefficient k between the transmitter and receiver coils remains constant once the vehicle is positioned. However, real-world deployment scenarios for solar-powered wireless charging are likely to include dynamic charging applications, where the vehicle moves across a series of transmitter pads embedded in the roadway [22]. In such dynamic cases, the coupling coefficient varies rapidly as the vehicle passes over each pad, and the time constant of the impedance matching controller in Equation 9 must be significantly shorter than the transit time over a single pad, which could be as brief as 0.5 to 2 seconds at highway speeds. The 8.5 ms settling time achieved in the present transient tests suggests that the control loop bandwidth is adequate for dynamic compensation, but the sensor sampling rate of 10 kHz and the computation delay of the microcontroller would need to be re-evaluated for a production-grade implementation operating at highway velocities.

A third limitation pertains to the efficiency of the intermediate charge-discharge cycle through the BESS. In the proposed architecture, every unit of solar energy that is eventually used to charge the vehicle battery is either directly consumed by the wireless transmitter or is first stored in the BESS and later discharged. The latter pathway incurs the round-trip efficiency losses of the battery, which for lithium-iron-phosphate chemistry typically range from 92 to 96% for a charging-discharging cycle at moderate rates [26]. Given that the diurnal simulation in Scenario D indicated that approximately 30% of the total solar energy harvested over a 24-hour period passed through the battery storage buffer, the overall system efficiency was reduced by roughly 1.2 to 2.4 percentage points compared to an ideal system with zero storage losses (i.e., a system where solar generation always perfectly matched the demand). While this penalty is modest, it represents an inherent trade-off of the buffered architecture. Future designs could mitigate this effect by optimizing the battery's operating state-of-charge window such that the discharge depth is minimized, or by employing hybrid energy storage systems that combine batteries with supercapacitors to handle transient mismatches while bypassing the battery for steady-state operation.

A. Operational Robustness, Foreign Object Detection, and Thermal Management Strategies

To transition the proposed hybrid architecture from a proof-of-concept prototype to a commercially viable product, the engineering challenges of operational robustness must be systematically addressed. The experimental prototype in this work was tested under controlled laboratory conditions with a fixed air gap and well-defined alignment scenarios. Reliable outdoor deployment, however, necessitates the integration of foreign object detection (FOD) and living object protection (LOP) systems that are mandatory under the SAE J2954 standard [16]. Metallic objects inadvertently placed between the transmitter and receiver coils can absorb radio frequency energy, leading to localized heating and potential fire hazards, while living organisms exposed to the magnetic field may experience induced currents beyond safety limits.

Several FOD approaches have been demonstrated in the literature, including quality factor degradation detection by observing the change in the resonant tank's damping factor [27], differential sensing through auxiliary sense coils that detect perturbations in the magnetic field [27], and thermal imaging using infrared cameras [27]. Among these, the quality factor detection method is most compatible with the proposed microcontroller-based energy management architecture because it can be implemented using the existing voltage and current sensors without additional hardware overhead. Specifically, the microcontroller can periodically inject a low-power probe signal into the transmitter coil and measure the decay rate of the resonant circuit's oscillation; a decrease in the quality factor below a calibrated threshold would indicate the presence of a foreign object. The implementation complexity is minimal, as the probe signal can be injected during the brief intervals between charging sessions without interrupting the primary power transfer.

Thermal management represents another critical consideration for a solar-powered charging system, particularly because the photovoltaic array itself generates significant heat under high irradiance, and the inverter's silicon carbide MOSFETs produce junction temperatures that can exceed 120°C under full load. The proposed architecture's BESS, being co-located with the power electronics, is particularly sensitive to elevated ambient temperatures, as lithium-iron-phosphate cells exhibit accelerated aging and reduced capacity when operated above 45°C [28]. A passive cooling strategy using aluminum heat sinks and natural convection may prove insufficient for the power levels targeted in commercial deployment. Forced air cooling, provided by a fan that draws power from the DC bus, could be integrated with a temperature-triggered control logic that activates the fan only when the heatsink temperature exceeds 60°C, thereby minimizing the parasitic power consumption. More advanced designs could employ a liquid cooling loop that circulates a dielectric coolant through cold plates attached to the inverter and the battery pack, with the waste heat potentially recovered for preheating the vehicle's cabin during winter charging sessions, thereby improving overall system utility.

B. Scalability Frameworks and Bidirectional Grid Interaction Potentials

Looking toward the future, the proposed hybrid architecture could be extended in two complementary directions: vertical scaling to higher power levels for fast charging applications, and horizontal scaling to enable bidirectional grid interaction for vehicle-to-grid (V2G) services. The vertical scaling challenge, as previously noted, involves increasing the power

throughput from 150 W to the 3.3–22 kW range typical of Level 2 charging, or even to 50–350 kW for fast and ultra-fast charging. A useful scalability framework can be derived by examining the scaling laws that govern the principal components. For the magnetic couplers, the mutual inductance M scales approximately as r^3 for circular coils with a fixed number of turns, where r is the coil radius [29]. Consequently, increasing the power by a factor of 100 would require increasing the coil radius by a factor of approximately $100^{1/3} \approx 4.6$, resulting in transmitter pads with diameters exceeding 1.5 m. This dimension becomes impractical for urban charging stations, suggesting that alternative coil geometries such as double-D or bipolar quadrature configurations, which offer better power density per unit area, should be explored [30].

For the BESS, the required capacity scales linearly with the desired energy throughput. A Level 2 charger delivering 7.2 kW of continuous power over a 4-hour charging session would deliver approximately 28.8 kWh of energy. To buffer the solar intermittency for such a session, the BESS should be sized to store the equivalent of at least one full charging session's worth of energy (28.8 kWh) plus an additional reserve of 20-30% for margin, resulting in a battery pack capacity of roughly 35–40 kWh. Such a battery would weigh approximately 250–300 kg using current lithium-iron-phosphate technology [26], imposing structural load requirements on the charging station's foundation. The volume would be on the order of 0.2–0.3 m^3, which is feasible within a standard parking lot enclosure but requires careful thermal and spatial planning.

The horizontal scaling direction, bidirectional grid interaction, represents a transformative opportunity to evolve the proposed charging station from a passive energy consumer into an active participant in the smart grid ecosystem. In a V2G configuration, the power electronics chain described in Section 4 could be reversed: when the vehicle is parked and the BESS is fully charged, the receiver coil could be driven as a transmitter to inject power back into the station's DC bus, where it could then be inverted by the high-frequency inverter operating in reverse to feed AC power into the local grid [31]. The key modification required for this capability is the replacement of the unidirectional synchronous rectifier on the vehicle side with a bidirectional rectifier-inverter module, and the replacement of the unidirectional BESS interface converter with a bidirectional DC-DC converter capable of both buck and boost operation. This configuration would enable the solar-powered charging station to function as a distributed energy resource, selling excess renewable energy back to the grid during peak demand periods.

The economic viability of such a V2G-enabled system depends on the frequency and magnitude of vehicle connection events, the time-of-use electricity tariff structure, and the battery degradation costs associated with the additional cycle count from V2G services. Preliminary modeling suggests that in a region with a substantial difference between peak and off-peak electricity prices (e.g., 30 cents/kWh versus 8 cents/kWh), a V2G-capable station could generate net revenue of \$500–800 per year per installed kW of inverter capacity [32]. When combined with the savings from using self-generated solar energy (approximately 1,500 kWh per year per kW of installed photovoltaic capacity in a temperate climate), the payback period for the proposed hybrid system could be reduced to 5–7 years, making it economically attractive relative to grid-tied wireless charging systems.

C. Pathways to Standardization and Techno-Economic Viability Analysis

For any wireless charging technology to achieve widespread adoption, adherence to interoperability standards is essential. The proposed hybrid architecture must, therefore, be designed to comply with the SAE J2954 standard, which specifies the operating frequency band (79–90 kHz), the allowable coil geometries (circular, double-D, and bipolar-quadrature), and the communication protocol between the ground-side and vehicle-side controllers [16]. Our prototype's 85 kHz operating frequency and the use of a circular coil geometry are consistent with the standard, but the communication protocol warrants further attention. The SAE J2954 standard mandates a low-power auxiliary communication channel, typically using a separate inductive link or a radio frequency module operating in the 2.4 GHz ISM band, to negotiate the power level, align the vehicle over the pad, and exchange safety status messages. In our architecture, this communication channel could be integrated into the energy management system's microcontroller, with the auxiliary link powered directly from the DC bus. A dedicated future work item is the design of a standards-compliant communication protocol that operates seamlessly with the solar-battery state-driven impedance matching control, ensuring that the vehicle can request a specific charging power level that the ground-side system can then deliver while respecting the current state of the BESS and the solar generation.
A comprehensive techno-economic analysis is needed to assess the viability of the proposed system in real-world deployment scenarios. The primary cost components include the photovoltaic array (currently\$0.30–0.50 per watt for utility-scale panels [33]), the battery energy storage system (\$200–300 per kWh for lithium-iron-phosphate packs [34]), the power electronics (inverters, converters, and controllers: approximately\$0.10–0.15 per watt [35]), and the coil assembly and shielding (\$200–500 per unit depending on size [36]). For a 7.2 kW Level 2 charging station with a 40 kWh BESS and a 8 kW photovoltaic array, the total component cost would be approximately\$8,000–12,000, yielding a cost per installed watt of \$1.11–1.67. This is competitive with commercially available DC fast charging stations, which cost\$0.50–1.20 per watt but do not include an energy buffer or a photovoltaic array [37]. The levelized cost of charging (LCOC) for this system, accounting for a 20-year lifespan, a 5% discount rate, and the declining cost of replacements (BESS replacement at year 10), is estimated at \$0.18–0.25 per kWh, which is comparable to or slightly lower than the retail price of grid electricity in many regions of the United States (\$0.12–0.30 per kWh). The inclusion of potential V2G revenue could further reduce the LCOC to \$0.12–0.18 per kWh, making the system economically self-sustaining.

Nevertheless, the economic analysis must also account for the parasitic power consumption of the energy management

system's microcontroller, the voltage and current sensors, and any active cooling fans. In the prototype, these parasitic loads accounted for 4.2 W, representing only 2.8% of the 150 W photovoltaic peak power. For a scaled 7.2 kW system, the parasitic consumption would scale to approximately 120–150 W, or about 1.6–2.1% of the rated power, a manageable overhead. A more significant economic consideration is the battery degradation caused by the additional cycle count from buffering solar intermittency. Most lithium-iron-phosphate batteries are warranted for 5,000–7,000 cycles to 80% depth of discharge [26]. Assuming daily cycling for 20 years (7,300 cycles), the BESS would need to be replaced once during the system's lifetime, adding$4,000–6,000 to the total cost of ownership. This replacement cost is already included in the LCOC estimate above.

VII. CONCLUSION

This paper has presented a hybrid solar-driven inductive power transfer architecture that enables sustainable contactless charging of electric vehicles by integrating a photovoltaic array with a mandatory battery energy storage buffer and a resonant wireless power transfer subsystem. The central contribution of this work is the demonstration that a localized energy storage system, interposed between the stochastic solar source and the high-frequency power conditioning unit, can effectively decouple the variable renewable generation from the deterministic requirements of wireless charging, thereby achieving stable power delivery independent of fluctuating irradiance conditions.

The experimental validation conducted on a scaled 150 W prototype yielded an end-to-end efficiency of 83.1% under aligned conditions at peak irradiance, which is within 2.1 percentage points of a comparable grid-tied wireless charging system. This near-parity in efficiency confirms that the elimination of grid connectivity does not impose a prohibitive performance penalty when the storage buffer is adequately sized and the voltage regulation is properly controlled. The transient response characterization further demonstrated that the battery-mediated voltage regulation can stabilize the DC bus within 8.5 ms following an 80% reduction in solar irradiance, maintaining a consistent inverter output and preserving wireless link efficiency at 89.4% throughout the event. The dynamic impedance matching control, driven by the composite solar-battery state vector, provided a 3.8 percentage point efficiency improvement under 100 mm lateral misalignment compared to fixed-frequency operation, validating the efficacy of integrating renewable source awareness into the wireless power transfer control loop.

The ablation study revealed that reducing the battery capacity by 50% or disabling active voltage regulation leads to substantial degradation in transient performance, with settling times increasing by factors of 2.6 and 17.1, respectively, and wireless link efficiency dropping by up to 10.3 percentage points. These findings underscore the critical importance of both adequate storage sizing and closed-loop voltage control for robust system operation.

While the current study confirms the technical feasibility of the proposed architecture at a reduced scale, several pathways for future work remain. Scaling the system to power levels suitable for practical electric vehicle charging, integrating foreign object detection and thermal management strategies, and exploring bidirectional grid interaction capabilities represent natural extensions of this research. The techno-economic analysis suggests that a 7.2 kW Level 2 charging station with a 40 kWh battery buffer and an 8 kW photovoltaic array could achieve a levelized cost of charging of $0.18–0.25 per kWh, potentially reduced further to$0.12–0.18 per kWh through vehicle-to-grid revenue. These economic projections, combined with the empirical performance demonstrated in this work, position the proposed hybrid architecture as a viable pathway toward fully autonomous, renewable-powered, contactless electric vehicle charging infrastructure that can contribute meaningfully to the decarbonization of transportation systems.

VIII. REFERENCES

1. Kene, R., Olwal, T., & Wyk, B. V. (2021). Sustainable electric vehicle transportation. *Sustainability*.
2. Micari, S., Polimeni, A., Napoli, G., Andaloro, L., et al. (2017). Electric vehicle charging infrastructure planning in a road network. *Renewable and Sustainable Energy Reviews*.
3. Joseph, P., Devaraj, E., & Gopal, A. (2019). Overview of wireless charging and vehicle-to-grid integration of electric vehicles using renewable energy for sustainable transportation. *IET Power Electronics*.
4. Hohm, D., & Ropp, M. (2003). Comparative study of maximum power point tracking algorithms. *Progress in Photovoltaics: Research and Applications*.
5. Tafticht, T., Agbossou, K., Doumbia, M., & Cheriti, A. (2008). An improved maximum power point tracking method for photovoltaic systems. *Renewable Energy*.
6. Kurs, A., Karalis, A., Moffatt, R., Joannopoulos, J., Fisher, P., et al. (2007). Wireless power transfer via strongly coupled magnetic resonances. *Science*.
7. Liu, X., Clare, L., Yuan, X., Wang, C., & Liu, J. (2017). A design method for making an LCC compensation two-coil wireless power transfer system more energy efficient than an SS counterpart. *Energies*.
8. Mumuni, Q., Ipinnimo, O., Obayiuwana, E., et al. (2025). Analysis of an inductive coupling-based solar-powered wireless charging station. *Journal of Integrated Science and Technology*.
9. Saraf, N., Pachkale, R., Sherkhane, M., et al. (2024). Solar powered wireless charging system for electric vehicles. In *2024 3rd International Conference on Power, Electronics and Computer Applications*.
10. Somefun, C., Oyelude, F., Somefun, T., et al. (2026). Design and construction of a solar powered dynamic wireless

charging system for electric vehicles. *Engineering Research Express*.
11. Shadoul, M., Abri, R. A., Yousef, H., et al. (2017). DC-DC boost converter controller design for PV applications. In *2017 9th IEEE-GCC Conference and Exhibition*.
12. Bartolucci, L., Cordiner, S., Mulone, V., & Santarelli, M. (2019). Hybrid renewable energy systems: Influence of short term forecasting on model predictive control performance. *Energy*.
13. Choi, J., Tsukiyama, D., Tsuruda, Y., et al. (2017). High-frequency, high-power resonant inverter with eGaN FET for wireless power transfer. *IEEE Transactions on Power Electronics*.
14. Arcos-Aviles, D., Pascual, J., Marroyo, L., et al. (2016). Fuzzy logic-based energy management system design for residential grid-connected microgrids. *IEEE Transactions on Smart Grid*.
15. Lim, Y., Tang, H., Lim, S., & Park, J. (2013). An adaptive impedance-matching network based on a novel capacitor matrix for wireless power transfer. *IEEE Transactions on Power Electronics*.
16. Samanchuen, T., Jirasereeamornkul, K., et al. (2019). A review of wireless power transfer for electric vehicles: Technologies and standards. In *2019 4th Technology Innovation Management and Engineering Science International Conference*.
17. Zhou, Y., & Li, X. (2015). Vehicle to grid technology: A review. In *2015 34th Chinese Control Conference (CCC)*.
18. Wang, C., Stielau, O., & Covic, G. (2005). Design considerations for a contactless electric vehicle battery charger. *IEEE Transactions on Industrial Electronics*.
19. Shariff, S., Alam, M., Ahmad, F., Rafat, Y., et al. (2019). System design and realization of a solar-powered electric vehicle charging station. *IEEE Systems Journal*.
20. Shahin, A., Abdelaziz, A., Houari, A., et al. (2024). A comprehensive analysis: Integrating renewable energy sources with wire/wireless EV charging systems for green mobility. *IEEE Access*.
21. Budhia, M., Covic, G., & Boys, J. (2011). Design and optimization of circular magnetic structures for lumped inductive power transfer systems. *IEEE Transactions on Power Electronics*.
22. Covic, G., & Boys, J. (2013). Modern trends in inductive power transfer for transportation applications. *IEEE Journal of Emerging and Selected Topics in Power Electronics*.
23. Al-Musawi, A. A. A., V, D. S., et al. (2024). Solar-driven wireless charging: Innovations in electric vehicle energy systems. In *E3S Web of Conferences*.
24. Arulvendhan, K., Nagaratnam, S., et al. (2024). Hybrid compensation based efficient wireless charging system design with solar photovoltaic interface toward sustainable transportation. *IEEE Transactions on Transportation Electrification*.
25. Chen, Q., Fan, F., Wang, J., & Chen, W. (2021). Core loss analysis and modeling of a magnetic coupling system in WPT for EVs. *World Electric Vehicle Journal*.
26. Wang, Y., et al. (2022). Optimal modeling and analysis of microgrid lithium iron phosphate battery energy storage system under different power supply states. *Journal of Power Sources*.
27. Lu, J., Zhu, G., & Mi, C. (2021). Foreign object detection in wireless power transfer systems. *IEEE Transactions on Industry Applications*.
28. Schimpe, M., von Kuepach, M., et al. (2018). Comprehensive modeling of temperature-dependent degradation mechanisms in lithium iron phosphate batteries. *Journal of The Electrochemical Society*.
29. Cirimele, V., Freschi, F., & Guglielmi, P. (2018). Scaling rules at constant frequency for resonant inductive power transfer systems for electric vehicles. *Energies*.
30. Jafari, H., Olowu, T., Mahmoudi, M., et al. (2021). Optimal design of IPT bipolar power pad for roadway-powered EV charging systems. *IEEE Canadian Journal of Electrical and Computer Engineering*.
31. Bertoluzzo, M., Giacomuzzi, S., & Kumar, A. (2021). Design of a bidirectional wireless power transfer system for vehicle-to-home applications. *Vehicles*.
32. Gomes, D., & Neto, R. (2024). Techno-economic analysis of vehicle-to-grid technology: Efficient integration of electric vehicles into the grid in Portugal. *Journal of Energy Storage*.
33. Cristea, M., Cristea, C., Tîrnovan, R., & Șerban, F. (2025). Levelized cost of energy (LCOE) of different photovoltaic technologies. *Applied Sciences*.
34. Lu, Y., & Zhu, T. (2024). Status and prospects of lithium iron phosphate manufacturing in the lithium battery industry. *MRS Communications*.
35. Xue, L., Galigekere, V., Gurpinar, E., Su, G., et al. (2023). Modular power electronics approach for high-power dynamic wireless charging system. *IEEE Transactions on Transportation Electrification*.
36. Jayalath, S., & Khan, A. (2020). Design, challenges, and trends of inductive power transfer couplers for electric vehicles: A review. *IEEE Journal of Emerging and Selected Topics in Power Electronics*.
37. Sawant, V., & Zambare, P. (2024). DC fast charging stations for electric vehicles: A review. *Energy Conversion and Economics*.